TECHNICAL ARTICLE

Simulation of Centimeter-Level Particle Motion Behavior in the Ruhrstahl–Heraeus Reactor Based on Situ Formation Micro-phase Molten Steel Purification Technology

XIN LIU,[1] YAN-PING BAO,[1,3] CHAO GU,[1] CHUN-JIE WU,[2] WEI KANG,[2] and HONG LI[2]

1.—State Key Lab of Advanced Metallurgy, University of Science & Technology Beijing, Beijing 100083, People's Republic of China. 2.—Anshan Iron & steel Group Company, Anshan 114014, People's Republic of China. 3.—e-mail: baoyp@ustb.edu.cn

In situ formation micro-phase molten steel purification technology is a new inclusions control technology. In this study, to increase the purification efficiency of the composite particles in the Ruhrstahl–Heraeus (RH) reactor, a water model was used to simulate the addition process of the spherical particles. The effects of gas flow rate and immersion depth on particle motion behavior were carefully investigated. The settling process of the particles in the reactor was further analyzed with kinetic theory. Industrial trials in a 180-t RH were also conducted to validate the effect of the composite particle treatment on steel quality. The results show that the small-size particles disperse more in the liquid steel. The gas flow rate is positively correlated with the settling displacement in this experimental range. The optimal gas flow rate is 4.1 $m^3 h^{-1}$, and the optimal immersion depth increases with increasing particle size. The results of the industrial trials also show that the quality of the steel treated with composite particles is significantly improved. The T·[O] content was reduced by 8.78 ppm. The inclusions number density was reduced by 3.55 pieces/mm^2. The percentage of inclusions smaller than 3 μm was increased from 27.02% to 73.96%.

INTRODUCTION

The key to clean steel production is to control inclusions. Inclusions in liquid steel can be removed by either aggregation and growth or bubble adsorption.[1–20] Ruhrstahl–Heraeus (RH) reactors offer excellent thermodynamic and kinetic conditions, and consist of a vacuum chamber, up and down snorkels, and a ladle. As argon is blown into the up-snorkel from the air hole, the liquid bulk density of the steel in the up-snorkel decreases, forcing this part of the molten steel into the vacuum chamber. Because of the shallow molten pool and high vacuum level (about 67 Pa) in the vacuum chamber, the gas in the molten steel escapes, and the degassed molten steel flows into the ladle via the down-snorkel, thus forming a molten steel circulation in the RH reactor.[3–6]

The basic idea of the situ formation micro-phase molten steel purification technology is to design a composite particle. The particles decompose at high temperature to release micro-bubbles and slag droplets.[7,8] Micro-bubbles can increase the probability of colliding with inclusions and improve the removal efficiency of inclusions.[9] At the steelmaking temperature, the carbonate powder will rapidly decompose to produce a large amount of CO_2. According to the ideal gas equation of state, huge pressure will be generated due to gas expansion, and the object around the carbonate will suffer from this pressure to form a burst reaction. Based on this mechanism, a composite particle has been designed, in which carbonates (such as $CaCO_3$, $MgCO_3$) are used as in situ generating agents for micro-bubbles.[10–12] After the reaction, CaO and MgO slag

droplets and micro-bubbles are generated, which collide with inclusions, then float upward, improving the inclusion removal efficiency.[13,14]

Many detailed studies have used water models to physically simulate RH refining processes.[15–18] Ladle bottom stirring enhanced the circulation of the RH degasser ladle system, increased the circulation flow rate, and reduced the mixing time.[19] Peixoto[20] stated that, by reducing the gas flow, the residence time of desulfurizing particles can be increased, also increasing the rate of desulfurization. Studies on water simulation of centimeter level particle motion behavior in RH are limited. The large size particle was more likely to float up to the interface of liquid and slag in the ladle before melting completely.[21]

In this study, water experiments were used to model the influence of the gas flow rate and immersion depth in a RH reactor on the particle motion behavior, and to select better process conditions. In addition, kinetic analysis was used to study the effects of increasing the flow velocity and vacuum level on the centimeter-level spherical particle motion behavior in the RH reactor. An industrial trial was conducted under optimal process conditions to study the effect of composite particle treatment on the quality of the steel, effective improvement of steel quality, and theoretical guidance for industrial production.

RESEARCH METHOD

Water Experimental Model

Experimental Equipment

A water experimental model of a 180-t RH reactor was established with a geometric ratio of 1:4, as shown in Fig. 1a. The model RH reactor and ladle were made of plexiglass. The molten steel and argon were simulated by water and compressed air, respectively. Polyethylene spherical particles simulated the composite particles. A vacuum bump was used to adjust the pressure in the vacuum chamber, and a U-tube manometer was used to measure the vacuum

chamber pressure. A rotameter was used to regulate the gas flow rate. A transition chamber was used to add spherical particles to a vacuum environment. In the experiments, water was added to the model according to Table I, and the snorkels' immersion depth and vacuum pressure were adjusted. Then, compressed air began to flow through the blowing port. After 10 min, 5-, 10-, and 15-mm polyethylene particles were added as tracers, and the change in the tracer position over time was evaluated based on the change in images captured by a camera. Table II shows the details of the experimental plan.

Experimental Principle

The water simulation model was based on kinetic and geometric similarity. The Reynolds number (Re) is a dimensionless number that can be used to characterize the fluid flow. When the Re exceeds the value specified in the self-modeling zone, the change of Re has almost no effect on the nature of the flow field, without ensuring that the Re is equal to meet the similarity principle.[21] $Re_m = 4.5 \times 10^5, Re_p = 1.5 \times 10^6$. The Re of both the prototype and the model are in the second self-modeling zone. Thus, to meet the requirements of dynamic similarity, it is only necessary to ensure that the Froude numbers of the two are equal,[22] as shown by Eq. (2):

$$Re = \frac{\rho v d}{\mu} \tag{1}$$

$$(Fr)_m = \frac{\rho_{Ar} v_m^2}{g d_m (\rho_{steel} - \rho_{Ar})} = \frac{\rho_{air} v_p^2}{g d_p (\rho_{water} - \rho_{air})} = (Fr)_p \tag{2}$$

where μ is the viscosity of surrounding fluid, Pa s; v is the density of the surrounding fluid, m s^{-1}; ρ is the density of surrounding fluid, kg m^{-3}; d is the feature length, ρ_{Ar} and ρ_{air} are the densities of argon and air, respectively, kg m^{-3}; v_p, and v_m are the fluid
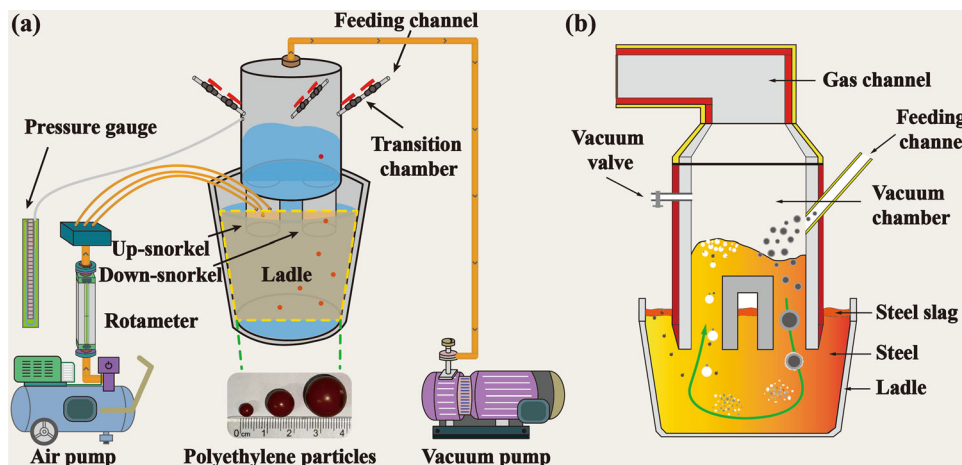

Fig. 1. Schematic of the RH reactor ladle model.

Table I. Parameters of prototype and model

Parameters	Prototype	Model
Ladle depth, mm	4340	1085
Upper internal diameter of ladle, mm	3000	750
Lower internal diameter of ladle, mm	2592	648
Internal diameter of snorkels, mm	560	140
Snorkels length, mm	1595	399
Vacuum chamber diameter, mm	1786	446.5
Vacuum chamber height, mm	5152	1288
Vacuum level, Pa	67	1000
Gas density, kg m^{-3}	1.784	1.205
Liquid density, kg m^{-3}	7000	1000
Particles density, kg m^{-3}	2100	990
Particles diameter, mm	15–20	5–15

Table II. Experimental plan

	Vacuum level, Pa	Gas flow rate (prototype), m^3 h^{-1}	Gas flow rate (model), m^3 h^{-1}	Immersion depth (prototype), mm	Immersion depth (model), mm	Particle diameters, mm
1	67	85	3	400	100	15, 10, 5
2	67	95	3.3	400	100	15, 10, 5
3	67	105	3.7	400	100	15, 10, 5
4	67	115	4.1	400	100	15, 10, 5
5	67	85	3	450	112.5	15, 10, 5
6	67	85	3	500	125	15, 10, 5
7	67	85	3	550	137.5	15, 10, 5
8	67	85	3	600	150	15, 10, 5
9	67	85	3	650	162.5	15, 10, 5

velocities of the prototype and model, respectively, m s^{-1}; g is the acceleration due to gravity, m s^{-2}; ρ_{steel} and ρ_{Ar} are the densities of molten steel and water, respectively, kg m^{-3}; and d_p, and d_m are the inner diameters of the snorkels used in the prototype and model, respectively, m.

The gas flow rate in the experiments model was calculated using Eq. (4):

$$\frac{L_m}{L_p} = \lambda = \frac{1}{4} \tag{3}$$

$$Q_m = \lambda^{2.5} Q_p \tag{4}$$

where L_p and L_m are the feature length of the prototype and model, respectively, m; and Q_p and Q_m are the flow rate of the prototype and model, respectively, m^3 h^{-1}. The feature lengths in this experiment are the diameter, height, and length of the RH water model and the actual equipment. The specific data are shown in Table I.

In the process of particle movement in the steel liquid, the main forces are buoyancy, viscous force, and surface tension, so this paper is based on the reflection of the liquid phase properties of the Morton number (Mo) equal The laboratory water

model can be used to simulate the actual RH equipment in the process of particle movement,[23] as shown by Eq. (5):

$$Mo = \frac{g \mu_c^4 \Delta\rho}{\rho_c^2 \sigma^3} \tag{5}$$

where μ_c is the viscosity of surrounding fluid, Pa s; ρ is the density of the surrounding fluid, kg m^{-3}; $\Delta\rho$ is the density difference between the two phases, kg m^{-3}; σ is the surface tension coefficient, N m^{-1}; and $\frac{1}{Mo_m} = 3.929 \times 10^{12}$, $\frac{1}{Mo_p} = 3.986 \times 10^{12}$. It has been proved that this experimental scheme can realistically simulate the particle motion process in the actual RH equipment.

Industrial Trial

Removal of micro-inclusions is by adding composite particles at the stable circulation stage after IF steel RH alloying; the particles are added by the alloy feeding channel after the alloying is finished, as shown in Fig. 1b. The composite particles are loaded into the high-level bin and, when the vacuum level is low enough, the particles are added and poured after 15 min of RH stable circulation. Sampling was at the RH outlet, the tundish, and the cast
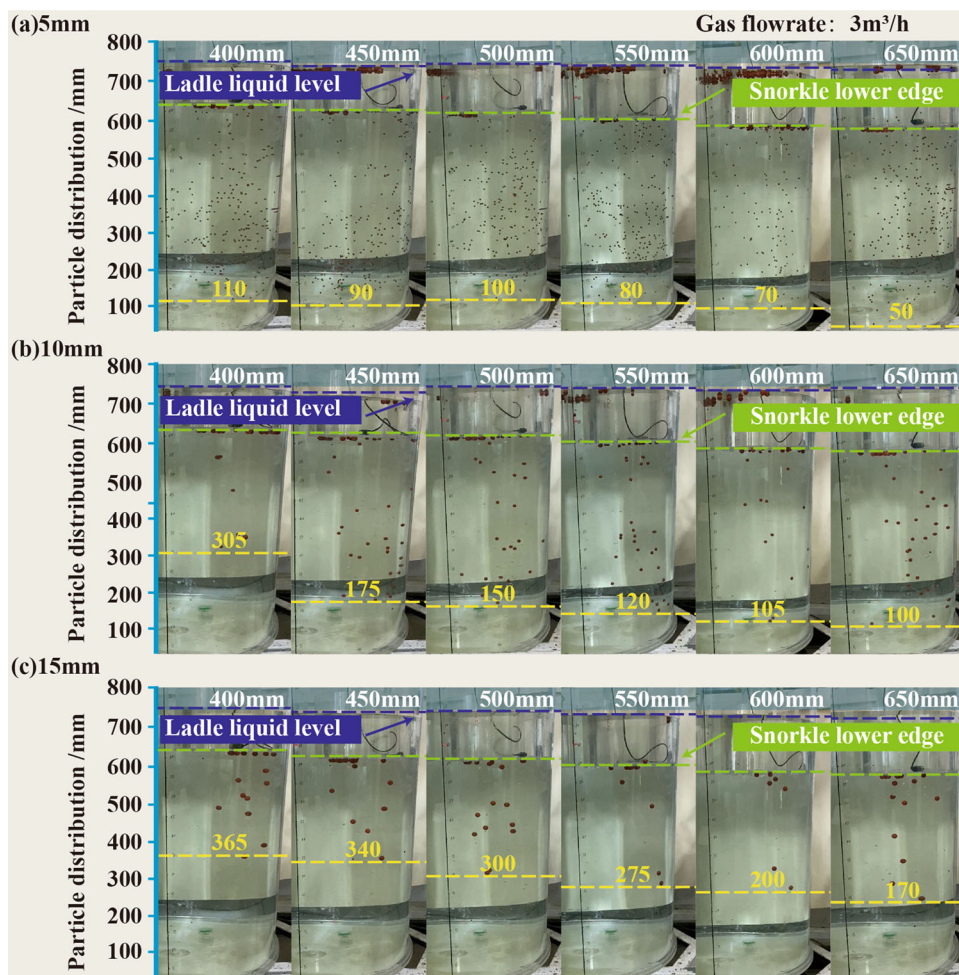
Fig. 2. Particle position distribution at 10 s for different immersion depths.

billets. The samples were made into a rod-sample ø5 × 50 mm, and the T·[O] content in the samples was determined by a nitrogen hydroxide analyzer (TCH-600; LECO, USA). The steel samples were made into 10 × 10 × 10 mm block samples, then ground and polished. An inclusion automatic system (EVO18; ZEISS, Germany) was used to analyze the number, size, and composition of inclusions in the detected area. S1 and S2 are without treatment comparison samples, and S3, S4, and S5 are the treated samples.

RESULTS AND DISCUSSION

Analysis of Water Experiments

Based on the study,[24] after the composite particles were added into the steel, the delayed bursting time is more than 10 s and more than 80% of the particles will undergo bursting behavior, so it is necessary to analyze the 10-s position distribution of the particles after entering the water. Figure 2 shows the results of the particle position distribution after 10 s of water entry at different immersion depths. During the experiments, the process parameters were adjusted to the target values and polyethylene particles were added after the RH circulation was stabilized. At a gas flow rate of 3.0 m³ h⁻¹, the effect on the 5-mm particle position distribution was less with increasing immersion depths. The reason is that, when the immersion depth is 100 mm, most of the 5-mm particles have settled near the bottom of the ladle, and, at this time, the 5-mm particles are diffusely distributed in the ladle, so the particle distribution range does not increase significantly in the subsequent experiments. For the 10- and 15-mm particles, the greater the immersion depths, the more diffusely the particles are distributed in the ladle. When the immersion depth is 600 mm, the deepest particle immersion depth has reached near the bottom of the ladle, while increasing the immersion depth to 650 mm has less effect on the particle immersion depth. Therefore, the particles' visible depth is similar between 600 and 650 mm. The images were taken at 10 s after the start of the experiment, most of the particles are moving in the liquid at this time, and a small number of particles have completed the settling process and float up to the bottom of the snorkels, so there is an evident interface existing in each figure.
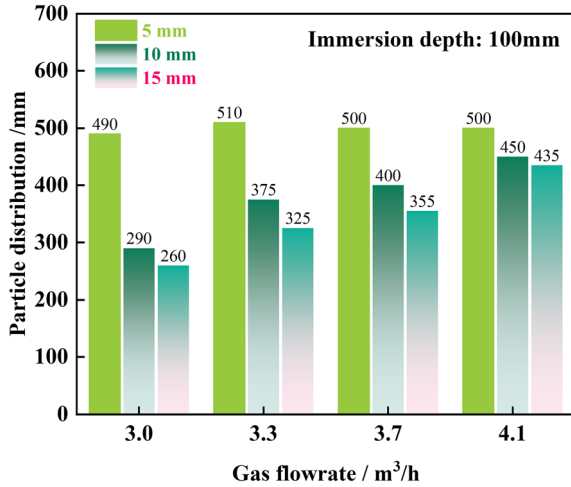
Fig. 3. Particle position distribution at 10 s for different gas flow rates.

Figure 3 shows the results of the particle position distribution after 10 s of water entry at different gas flow rates. At the model immersion depth of 100 mm, the gas flow rate has less effect on the distribution position of the 5-mm particles at 10 s. For the same reason as in Fig. 2a, the smaller-sized particles are diffusely distributed in the steel solution. The settling distance of the 10- and 15-mm particles in the liquid increases with the increase of the gas flow rates.

Figure 4 shows the straight line fitted according to the experimental data, the value of K is the rate constant of particle settling displacement with respect to the change of gas flow rate, and R^2 evaluates the accuracy of the slope of the fitted line (the closer to 1, the higher the accuracy). The results show a good and positive correlation between the gas flow rate and the particle settling displacement, and the higher the gas flow rate, the greater the settling displacement. The settling displacement of the 5-mm particles increased from 550 mm to 590 mm and that of the 15-mm particles increased from 160 mm to 500 mm when the gas flow rate increased from 3.0 m^3 h^{-1} to 4.1 m^3 h^{-1}. The 5-mm particles have the largest settling displacement in the whole process, because the large-sized particles need to overcome greater resistance in the settling process, and the velocity decreases sharply, resulting in a relatively low settling displacement.

As the immersion depth increases, the particle settling displacement of the 5-mm particles slowly increases, while the settling displacement of the 10-mm and 15-mm particles first increases and then decreases. When the particle size is 10 mm, the maximum particle settling displacement is 137.5 mm immersion depth. When the particle size is 15 mm, the maximum particle settling displacement is 150 mm immersion depth. The optimal immersion depth increases with increasing particle size, as shown in Fig. 5.

The results of particle settling time are shown in Fig. 6. The gas flow rate increases, the liquid flow rate in the ladle increases, and the particle settling time is slowly shortened. The settling time of the 5-, 10-, and 15-mm particles increases with increasing size for different process parameters. The small-sized particle settling process resistance is smaller, the movement velocity is relatively fast, so the settling time is short. When the gas flow rate is certain, the immersion depth increases, and the particle settling time shows a trend of first rising and then falling. From the above results, it can be seen that the small particle size has the highest degree of dispersion in the ladle under different working conditions, producing a wider range of fine bubbles and slag particles during bursting, and adsorbing inclusions more effectively.

Theoretical Calculation

The forces on the particles during its movement in the RH reactor are shown in Fig. 7. The particle falling can be divided into three processes: (1) falling process in vacuum chamber; (2) entering the liquid steel; and (3) settling process in the steel.

Falling Process in Vacuum Chamber

The equation of motion during the falling process in vacuum chamber can be described by Newton's second law:

$$\rho_B \cdot \frac{4}{3}\pi R_B^3 \cdot g - P_r \cdot 2\pi R_B^2 = \rho_B \cdot \frac{4}{3}\pi R_B^3 \cdot a \qquad (6)$$

$$s_1 = \frac{1}{2}at_1^2 \qquad (7)$$

$$v_1 = at_1 \qquad (8)$$

where, ρ_B and R are the density and diameter of the particle, respectively, kg m^{-3}, m; g is the acceleration of gravity, taken as 9.801 m s^{-2}; P_r is the vacuum level of the vacuum chamber, Pa; and s is the distance from the bin to the surface of the steel, taken as s = 5 m.

Figure 8a shows the relationship curve between the particle velocity and size during the falling process in a vacuum chamber. At a certain vacuum level and particle density, the falling velocity of the particle gradually increases with the size, and this situation is especially obvious for small particles. Due to the effect of drag, the velocity of the particle when it reaches the surface of the steel will decrease as the vacuum level decreases. When the vacuum level is 67 Pa, the velocity of the 10-mm composite particle is 6.09 m/s when it reaches the steel surface, while, when the vacuum level becomes 100 Pa, the velocity drops to 2.67 m/s. Therefore, it is crucial that the RH vacuum level is appropriate for the composite particles to effectively enter the liquid steel.
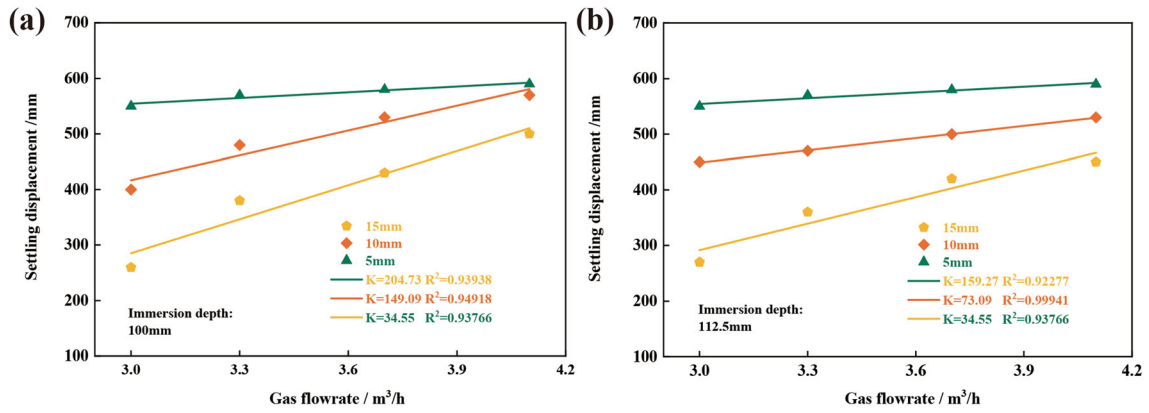
Fig. 4. Particle settling displacement at immersion depths of (a) 100 mm and (b) 112.5 mm.
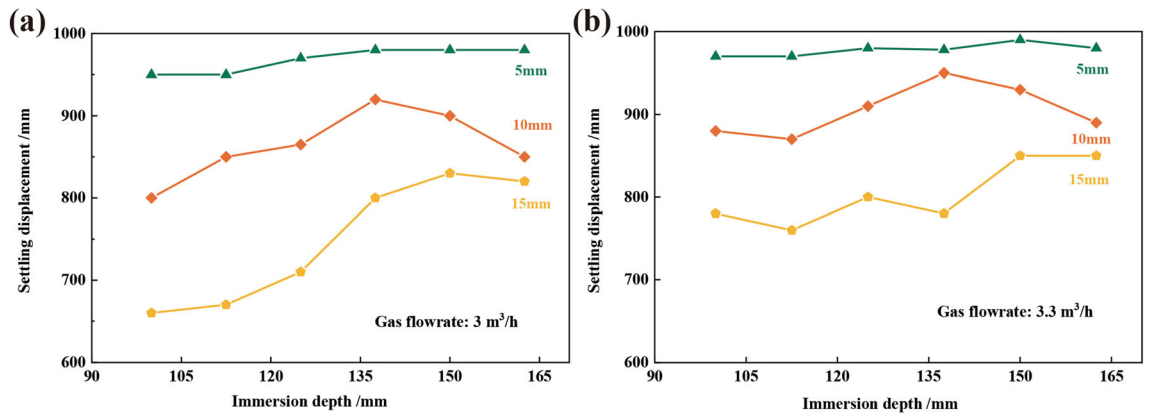

Fig. 5. Particle settling displacement in gas flow rate of (a) 3.0 m³ h⁻¹ and (b) 3.3 m³ h⁻¹.
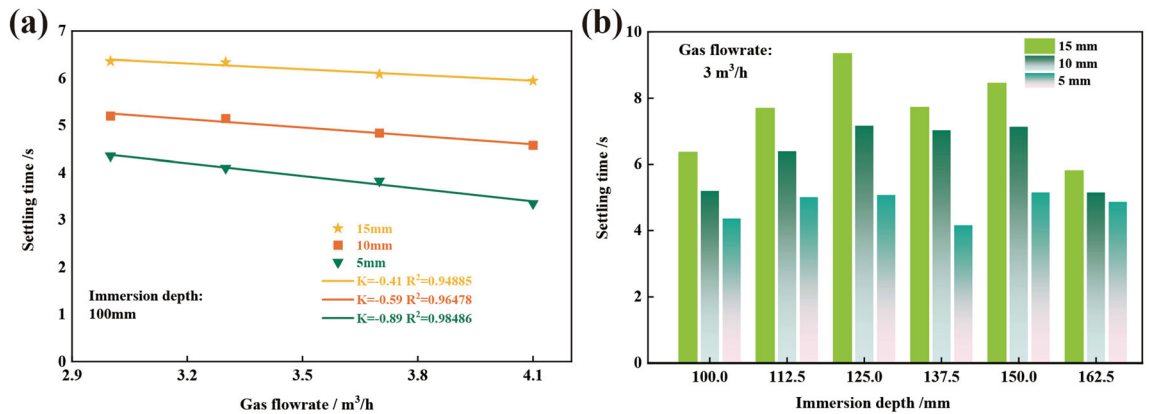

Fig. 6. Particle settling time in (a) immersion depth 100 mm and (b) gas flow rate 3.0 m³ h⁻¹.

Entering the Liquid Steel

The motion equation of the composite particle in the process of entering the liquid steel is[25–28]:

$$m_B \frac{dv}{dt} = F_d + F_b + F_S \qquad (9)$$

$$F_d = C_d \alpha_B \rho_m \frac{v^2}{2} \qquad (10)$$

$$F_b = \frac{4}{3} \pi R_B^3 g (\rho_m - \rho_B) \qquad (11)$$

$$F_S = \frac{dE_\sigma}{dh_B} = \frac{\sigma_m d_s}{dh_B} \qquad (12)$$

where v is the instantaneous velocity of the particle during the entering, m s⁻¹; m_B is the particle mass, kg; $F_d, F_b,$ and F_S are, respectively, the resistance of

the liquid steel to the particle, the gravity considering buoyancy, and the interfacial resistance of the new interface formed when the particle enters the liquid steel, N; C_d is the drag coefficient, which is taken as $C_d = 0.45$ in this study for turbulent zone settling; α_B is the maximum cross − sectional area of the particle, $\alpha_B = \pi R_B^2$, m^2; ρ_m and ρ_B are the densities of the steel and the particle, respectively, taking $\rho_m = 7000$ kg m^{-3}, and $\rho_B = 3300$ kg m^{-3}; dE_σ is the change in the interfacial energy of the metal when the particle enters at a depth of dh_B; σ_m is the interfacial tension of the liquid steel, taking $\sigma_m = 1.2$

N m^{-1}; and d_s is the change of interfacial energy when the composite particle enters the liquid steel. The particle forms a cylindrical channel when it enters the steel. The diameter of the channel is equal to the diameter of the composite particle $2R_B$, $d_s = 2\pi R_B dh_B$, substituted into Eq. (9):

$$\frac{dv}{dt} = -\frac{3C_d \alpha_B \rho_m}{8\pi R_B^3 \rho_B} - \frac{3\sigma_m}{2R_B^2 \rho_B}\left[\frac{2g(\rho_m - \rho_B)}{3\sigma_m} - 1\right] \quad (13)$$

$$\int_{v_2}^{v} 1 dv = \int_0^t -\frac{3C_d \alpha_B \rho_m}{8\pi R_B^3 \rho_B} - \frac{3\sigma_m}{2R_B^2 \rho_B}\left[\frac{2g(\rho_m - \rho_B)}{3\sigma_m}\right.$$
$$\left. - 1\right]dt$$
$$\quad (14)$$

$$h_B = \int_0^t v dt \quad (15)$$

The critical state of the composite particle into the steel is the entry depth, $h_B = 2R_B$, Its full kinetic energy is used to overcome the energy barrier when entering the steel, $v = 0$, obtained from:

$$v_2 = 2R_B^{-\frac{1}{2}}\sqrt{\frac{\sigma_m}{C_d \rho_m}\left(e^{\frac{3C_d \rho_m}{2\rho_B}} - 1\right)} \quad (16)$$
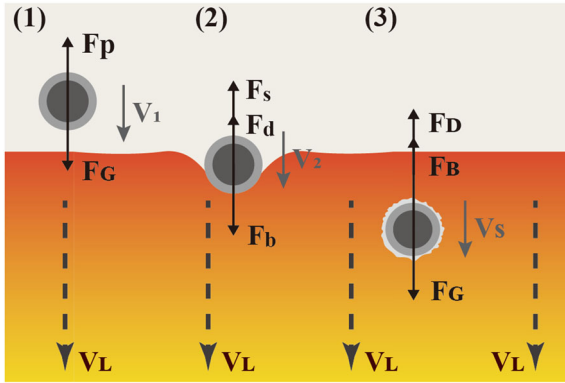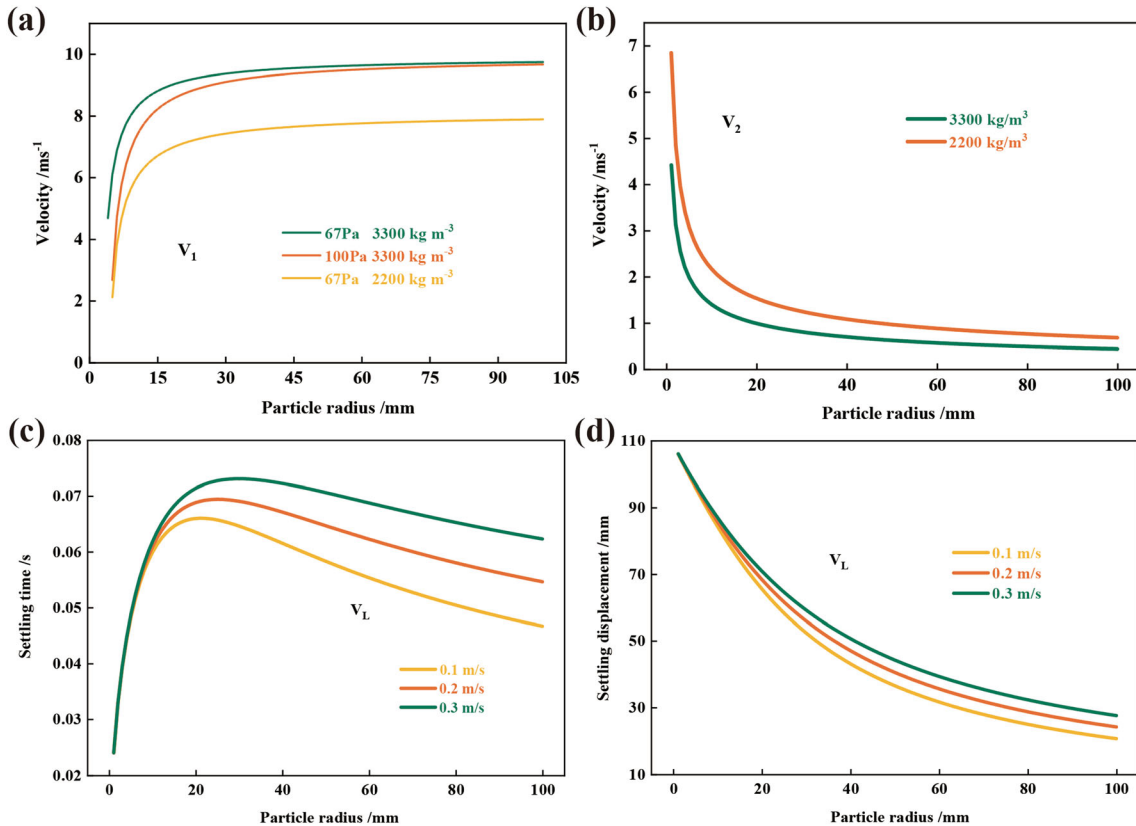

Fig. 7. Force analysis.

Fig. 8. (a) Relationship curve between the particle velocity and size during the falling process; (b) relationship between v_2 and particle density; relationship between particle size and (c) settling time (d) settling displacement.

Simulation of Centimeter-Level Particle Motion Behavior in the Ruhrstahl–Heraeus Reactor
Based on Situ Formation Micro-phase Molten Steel Purification Technology

3731

Figure 8b shows the relationship between the velocity, v_2, and particle size after it enters the molten steel. In the case of a certain density of the particle, the size of the composite particle has a large effect on its critical entry velocity. The smaller the particle size, the larger the critical entry velocity. As the particle size becomes larger, the particle weight increases and the momentum increases, so the critical entry velocity of the larger size particle is relatively small.

Settling Process in the Steel

Particle settling forces in liquid flow fields can be divided into three categories according to the mode of action of the forces[29]: (1) forces unrelated to the relative motion between the fluid and the particles, including pressure gradient forces, gravity, etc., (2) forces that depend on the relative motion between the fluid and the particles and are in the same direction as the relative velocity of motion, including Stokes viscous drag, Basset force, etc., and (3) Forces that depend on the relative motion between the fluid and the particles, but are perpendicular to the direction of the relative motion velocity, such as Saffman force, Magnus force, etc. When $d_B > 0.05$ mm, the Saffman force, Magnus force, and Stokes resistance are of the same magnitude and can be ignored.[30] Therefore, the computational model in this study considers only the pressure gradient forces, gravity, and Stokes resistance. Assuming that the particle force, fluid flow rate, and velocity of motion upward is positive, the equation of motion is[31]:

$$F_G + F_P + F_D = m_B \frac{dv_s}{dt} \quad (17)$$

$$F_G = \frac{4}{3}\pi R_B^3 \rho_B g \quad (18)$$

$$F_P = \frac{4}{3}\pi R_B^3 \rho_m g \quad (19)$$

$$F_D = \frac{1}{2}\pi R_B^2 \rho_m C_d (v_L + v_s)^2 \quad (20)$$

$$R_e = \frac{2(v_L + v_s)R_B \rho_m}{\mu_m} \quad (21)$$

where $F_G, F_P,$ and F_D are, respectively, the gravitational forces, pressure gradient forces, and Stokes viscous drag, N; μ_m is the fluid kinematic viscosity, Pa s^{-1}; v_L is the steel flow velocity, direction downward, m s^{-1}; v_s is the particle motion velocity, direction downward, m s^{-1}; and $\rho_B < \rho_m$, the direction of the combined force is opposite to the direction of motion, and the particle is in decelerating motion:

$$dt = \frac{2R_B \rho_B}{\frac{3}{4}\rho_m C_d (v_L + v_s)^2 - 2R_B g(\rho_B - \rho_m)}dv_s \quad (22)$$

The particle settling end velocity is 0:

$$\int_0^t 1 dt = \int_{v_2}^0 \frac{2R_B \rho_B}{\frac{3}{4}\rho_m C_d (v_L + v_s)^2 - 2R_B g(\rho_B - \rho_m)}dv_s \quad (23)$$

$$t = 4\rho_B \sqrt{\frac{R_B}{6\rho_m C_d g(\rho_B - \rho_m)}} arctan(\sqrt{\frac{3\rho_m C_d}{8R_B g(\rho_B - \rho_m)}}(v_L + v_2)) \quad (24)$$

$$s = v_s \cdot t \quad (25)$$

The settling time and settling displacement of the composite particles in the liquid steel can be calculated according to Eqs. (22)–(25), as shown in Fig. 8c and d. When the particle diameter is less than 20 mm, the particle settling time in the steel increases rapidly with the increase of the particle diameter, which is consistent with the experimental results. For particles with diameters greater than 20 mm, the settling time slowly decreases as the particle diameter increases. Large-sized composite particles need to overcome greater resistance in the settling process, so, when the composite particle enters the steel, its settling velocity decreases sharply, leading to a decrease in settling time. The initial velocity of small-sized particles is larger and the settling time is longer, so the settling displacement of the particles in the steel solution decreases with the increase of the particle diameter.

Analysis of Industrial Trial

Figure 9 shows a diagram of the industrial trial process. Based on the above experimental results, the 15-mm composite particles were added to the RH using a gas flow rate of 115 m^3 h^{-1} and an immersion depth of 400 mm. The addition of composite particles to the steel during the RH refining process can significantly reduce the T·[O] of the steel, with 35 ppm of T·[O] in the untreated RH sample and an average of 26.22 ppm of T·[O] after treatment. The T·[O] of the tundish and the cast billet were significantly reduced, as shown in Fig. 10a.

The analysis of the inclusions in the billets showed that the number density of inclusions in the billets treated with composite particles was reduced and the percentage area of inclusions was significantly lower, as shown in Fig. 10b and c. The number density of inclusions was reduced from a maximum of 5.50 pieces/mm^2 to a minimum of 1.95 pieces/mm^2, and the area percentage content of inclusions was reduced from a maximum of
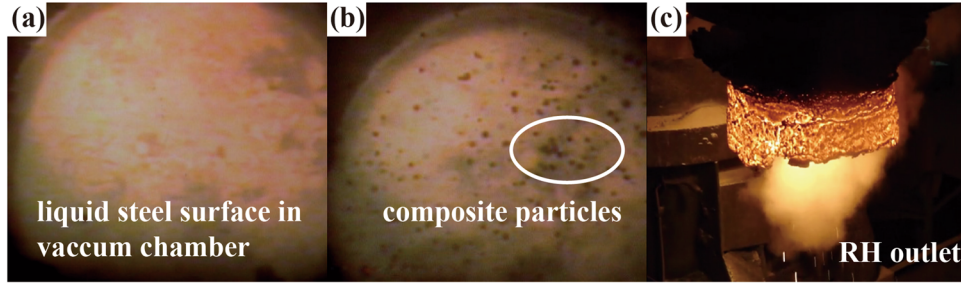
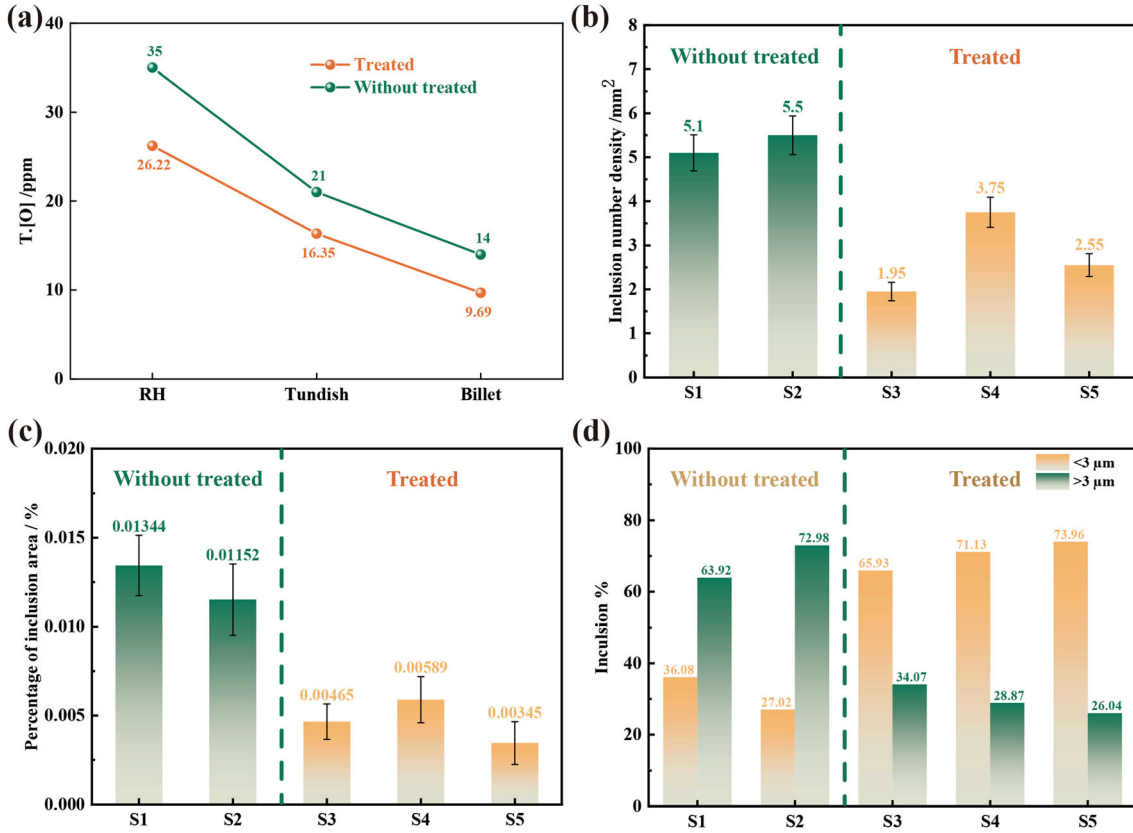Fig. 9. (a) Liquid steel surface; (b) feeding composite particles; (c) RH outlet.

Fig. 10. Composite particle treatment and comparison samples of (a) changes in T·[O] content; (b) inclusion number density; (c) percentage of inclusion area; (d) changes in inclusion size.

0.01344% to 0.00345%. The size distribution of the inclusions is significantly reduced, the percentage of inclusions of < 3 μm in the comparison sample was 27.02%, and the percentage of inclusions of < 3 μm after the composite particle treatment was 73.96%. Accordingly, the number of large-sized oxide inclusions was significantly reduced, with > 3-μm oxide inclusions accounting for 34.07% or less, as shown in Fig. 10d. The composite particle treatment is able to reduce the T·[O] content and the number size of inclusions in the steel.

CONCLUSION

Based on Ansteel's technology of in situ formation micro-phase molten steel purification, a water model was developed to study the effects of gas flow rate and immersion depth in the RH reactor on the motion behavior of particles in the liquid steel. Under these conditions, the effect of composite particle treatment on steel quality at optimum gas flow rate and immersion depth was investigated by an industrial trial. The main results of this study are summarized as follows:

1. Small-sized particles disperse more in the liquid steel. The settling process of large-sized particles needs to overcome greater resistance, and the settling velocity decreases sharply, so the settling time is longer and the settling displacement is shorter. The actual production should use the smaller-sized composite particles.

2. The particle settling displacement increases with the increase of the gas flow rate, and the optimal gas flow rate is $4.1 \, \mathrm{m}^3 \, \mathrm{h}^{-1}$. The optimum immersion depth increases with particle size, and the suitable immersion depth is 100 mm.

3. Under optimal process conditions, the T·[O] content in the cast billets after the composite particle treatment reached less than 10 ppm, the inclusion number density was reduced by 3.55 pieces/mm^2, and the percentage of < 3-μm inclusions in the billets increased by 46.94%, significantly improving the steel product quality.

CONFLICT OF INTEREST

On behalf of all authors, the corresponding author states that there is no conflict of interest.

ACKNOWLEDGEMENTS

REFERENCES

1. S.F. Chen, H. Lei, H.C. Hou, C.Y. Ding, H. Zhang, and Y. Zhao, *J. Mater. Res. Technol.* 15, 5141 (2021).
2. H. Wang, Y.P. Bao, J.G. Zhi, C.Y. Duan, S. Gao, and M. Wang, *ISIJ Int.* 61, 657 (2021).
3. B.S. Liu, G.S. Zhu, H.X. Li, B.H. Li, and A.M. Cui, *Int. J. Min. Met. Mater.* 17, 22 (2010).
4. X.G. Ai, Y.P. Bao, W. Jiang, J.H. Liu, P.H. Li, and T.Q. Li, *Int. J. Min. Met. Mater.* 17, 17 (2010).
5. F. Jiang, and G.G. Cheng, *Ironmak. Steelmak.* 39, 386 (2012).
6. Y.H. Li, Y.P. Bao, R. Wang, L.F. Ma, and J.S. Liu, *Int. J. Min. Met. Mater.* 25, 153 (2018).
7. F.P. Tang, Z. Li, X.F. Wang, B.W. Chen, and P. Fei, *Int. J. Min. Met. Mater.* 18, 144 (2011).
8. F.P. Tang, X.F. Wang, Z. Li, Y. Lin, B.W. Chen, and P. Fei, *Ironmak. Steelmak.* 38, 285 (2011).
9. L. Wang, H.G. Lee, and P. Hayes, *ISIJ Int.* 36, 7 (1996).
10. S. Chang, Z. Zou, B. Li, M. Isac, and R.I. Guthrie, *Metall. Mater. Trans. B.* 53, 526 (2022).
11. R. Guthrie, and M. Isac, *In Extraction.* 729, 1 (2018).
12. S. Chang, X. Cao, C.H. Hsin, Z. Zou, M. Isac, and R. Guthrie, *ISIJ Int.* 56, 1188 (2016).
13. L. Wang, S. Yang, J. Li, S. Zhang, and J. Ju, *Metall. Mater. Trans. B.* 48, 805 (2017).
14. Y. Xiao, G. Wang, H. Lei, and S. Sridhar, *J. Alloy Compd.* 813, 1543 (2020).
15. B. Zhu, K. Chattopadhyay, X. Hu, B. Zhang, Q. Liu, and Z. Chen, *Vacuum* 152, 30 (2018).
16. X. Li, X. Wang, Y.P. Bao, J. Gong, and M. Wang, *JOM.* 72, 3628 (2020).
17. J. Dong, C. Feng, R. Zhu, G. Wei, J. Jiang, and S. Chen, *Metall. Mater. Trans. B.* 52, 2127 (2021).
18. C. Yao, M. Wang, Y.J. Ni, J. Gong, L.D. Xing, H.B. Zhang, and Y.P. Bao, *JOM.* 1, 1 (2022).
19. R.D. Wang, Y. Jin, and H. Cui, *Metall. Mater. Trans. B.* 53, 342 (2022).
20. J.J.M. Peixoto, W.V. Gabriel, T.A.S. de Oliveira, C.A. da Silva, I.A. da Silva, and V. Seshadri, *Metall. Mater. Trans B.* 49, 2421 (2018).
21. W.B. Rauen, B. Lin, R.A. Falconer, and E.C. Teixeira, *Chem. Eng. J.* 137, 550 (2008).
22. C.A. Da Silva, I.A. Da Silva, E.M. de Castro Martins, V. Seshadri, C.A. Perim and G.A. Vargas Filho, *Ironmak Steelmak.* 31, 37 (2004).
23. B. Dahya, and M.E. Weber, *J. Fluid Mech.* 105, 61 (1981).
24. F.P. Tang, Z. Li, X.F. Wang, W.S. Liu, and B.W. Chen, *Iron Steel.* 45, 28 (2010).
25. A.N. Ernest, J.S. Bonner, and R.L. Autenrieth, *J. Environ. Eng.* 121, 320 (1995).
26. M.E. ONeill, *Chem Eng Sci.* 23, 1293 (1968).
27. S. Taniguchi, *ISIJ Int.* 36, 117 (1999).
28. H. Matsuno, *CAMP.* 10, 103 (1997).
29. D.Y. Liu, *Beijing: Higher Education Press.* (1993).
30. S.H. Huang, W. Li, and L.J. Cheng, *Appl. Math. Mech.* 21, 265 (2000).
31. C.Y. Dong, W.L. Luan, S.T. Zhou, and Q. Zhang, *J. China Univ. Pet. (Ed. Nat. Sci.).* 31, 55 (2007).